PAPER

Fast pseudocapacitive reactions of three-dimensional manganese dioxide structures synthesized *via* self-limited redox deposition on microwave-expanded graphite oxide†

Wencong Zeng,[a] Yuan Zhao,[a] Kun Ni[a] and Yanwu Zhu*[ab]

Three-dimensional (3D) MnO_2 structures are deposited on microwave-expanded graphite oxide (MEGO) *via* a self-limited redox reaction between MEGO and $KMnO_4$. The 3D architecture consists of MnO_2 sheets lying uniformly on MEGO and walls protruding from MEGO, both with thickness in the range of 1–5 nm. The loading of MnO_2 and the height and density of walls in the 3D architecture can be controlled by tuning the reaction duration, leading to a balanced specific capacitance and power performance. Symmetric supercapacitors assembled using a MEGO–MnO_2 composite with 24.5 wt% MnO_2 can work at a voltage of up to 2 V in a 1 M Na_2SO_4 electrolyte, yielding an energy density of 14 W h kg^{-1} (13.6 W h L^{-1}) at a power density of 250 W kg^{-1} (243 W L^{-1}) or a power density of 7.67 kW kg^{-1} (7.44 kW L^{-1}) at an energy density of 5.46 W h kg^{-1} (5.3 W h L^{-1}). Asymmetric supercapacitors, consisting of the MEGO–MnO_2 (containing 24.5 wt% MnO_2) composite as the positive electrode and activated MEGO as the negative electrode in a 1 M Na_2SO_4 electrolyte, exhibit an energy density of 25.1 W h kg^{-1} at a power density of 93 W kg^{-1} with a working voltage of up to 1.8 V.

1. Introduction

Supercapacitors (SCs), also known as electrochemical capacitors, have emerged as promising candidates for energy storage as they have long cycle lives and can provide high power density and excellent pulse charge and discharge.[1–3] Based on their charge-storage mechanism, SCs can be classified into two basic types: electric-double-layer capacitors (EDLCs), which mainly employ porous carbon materials as electrodes; pseudocapacitors, which use metal oxides or conducting polymers as electrodes.[4–6] Pseudocapacitive transition-metal oxides such as RuO_2, NiO, and MnO_2 have been extensively studied as active materials in electrodes for SCs owing to large pseudocapacitance based on fast and reversible redox reactions at the electrode surface, which result in large specific capacitances exceeding those of carbon-based materials in electric-double-layer charge storage.[7–9]

Among the pseudocapacitive oxides mentioned above, manganese oxide is characterized as a low-cost material with a large theoretical capacity (1370 F g^{-1}), abundant resources, and environmentally friendly nature, and it has attracted significant interest as a promising electrode material for SCs.[10,11] Owing to the poor conductivity of intrinsic MnO_2, it has been combined with highly conductive materials such as carbon to form composites with improved conductivity and electrochemical performance.[12–15] Of the various carbon-based materials, graphene is especially attractive to researchers in many fields because of its large theoretical specific surface area (~2630 m^2 g^{-1}), high conductivity, excellent mechanical flexibility, light weight, and chemical stability, as well as feasibility for large-scale production.[16–18]

In general, MnO_2–graphene composites can be synthesized by physically mixing MnO_2 with carbon, or by electrochemically or chemically depositing MnO_2 on carbon. Among the chemical-deposition methods, synthesis of MnO_2 through the self-limited redox reaction between $KMnO_4$ and carbon is an effective way to enhance the MnO_2 utilization ratio and optimize the capacitance of composites.[19–24] For example, Wei *et al.* obtained a MnO_2–graphene composite by self-limited deposition of nanoscale particle-like MnO_2 on the surface of chemically reduced graphene oxide under microwave irradiation.[25] Dong *et al.* prepared nanoflower-like MnO_2 on graphene foam *via* the redox reaction of $KMnO_4$ with carbon under hydrothermal conditions, and the resulting composite demonstrated

[a]Key Laboratory of Materials for Energy Conversion, Chinese Academy of Sciences, Department of Materials Science and Engineering, University of Science and Technology of China, Hefei, Anhui 230026, P. R. China. E-mail: zhuyanwu@ustc.edu.cn

[b]iChEM (Collaborative Innovation Center of Chemistry for Energy Materials), University of Science and Technology of China, Hefei, Anhui 230026, P. R. China

† Electronic supplementary information (ESI) available: TGA data, Raman spectroscopy results, and TEM images of MEGO and MEGO–MnO_2 composites; CV curves, specific capacitance, and galvanostatic charge–discharge curves of GMn-*x* symmetric and asymmetric SCs. See DOI: 10.1039/c5ra24104a

good performance for SCs.[26] Typical MnO_2 nanoparticles obtained from the reaction of $KMnO_4$ with graphene materials are usually sparsely distributed on carbon and thus have relatively poor ion diffusion or weak electrical connection with carbon, which is undesirable for high power output. In contrast, thin MnO_2 nanosheets (with thickness of the order of a few nanometers) that are closely connected with the carbon skeleton may have fast ion diffusion and low internal resistance because the pseudocapacitive reaction is considered to mainly occur at a depth of less than 5 nm from the MnO_2 surface.[27–30] Thus, it is desirable to develop sub-5-nm sheet-like MnO_2 on carbon for MnO_2–carbon composite SCs with superior performance.

In this work, a straightforward strategy is proposed to synthesize three-dimensional (3D) MnO_2 structures on microwave-expanded graphite oxide (MEGO) *via* the reaction between MEGO and $KMnO_4$. Owing to the self-limited reaction, the nanosheets lying on graphene had a thickness of only several nanometers, while the density and height of MnO_2 walls in 3D MnO_2 structures increased with the synthesis duration, forming a porous honeycomb morphology on MEGO. This 3D MnO_2 structure benefitted the contact between the electrolyte and MnO_2, as well as the electron transfer between MnO_2 and graphene, leading to more efficient utilization of MnO_2. Asymmetric supercapacitors employing a MEGO–MnO_2 composite (MnO_2 loading: 24.5 wt%) as the positive electrode and activated MEGO (aMEGO) as the negative electrode in an aqueous 1 M Na_2SO_4 electrolyte had an operating voltage of up to 1.8 V, resulting in an energy density of 25.1 W h kg^{-1} at an averaged power density of 93 W kg^{-1} and fast frequency response, as observed in Nyquist plots. In addition, the asymmetric supercapacitors exhibited retention of 78% of the specific capacitance after 5000 cycles.

2. Experimental

2.1 Material synthesis

MEGO was prepared by treating graphite oxide powder under microwave irradiation, and aMEGO was synthesized by KOH activation of MEGO; the synthesis procedures of both materials are described in our previous work.[31,32] MEGO–MnO_2 composites were synthesized using a self-limited redox deposition process based on the reaction between MEGO and $KMnO_4$. In brief, 100 mg MEGO powder was added to 500 mL diluted aqueous $KMnO_4$ solution (10 mM) under magnetic stirring. During the reaction, the solution temperature was kept at 30 °C. The mixtures were vacuum-filtered and washed after the reaction, followed by drying in air at 60 °C for 10 h. The samples were further dried in vacuum at 80 °C for 9 h. The reaction duration was controlled to be 10, 40, or 120 min; hereafter, the corresponding MEGO–MnO_2 composites obtained from the reactions are referred to as GMn-x (x = 10, 40, 120).

2.2 Characterizations

Scanning electron microscopy (SEM) images were collected on a scanning electron microscope (JSM-6700M, JEOL, Japan). Transmission electron microscopy (TEM) and high-resolution

TEM (HRTEM) images were obtained on a transmission electron microscope (JEM-2100, JEOL, Japan) using an accelerating voltage of 200 kV. Thermogravimetric analysis (TGA) was carried out using a TG analyzer (DTG-60H, Shimadzu, Japan) under flowing air and at a heating rate of 10 °C min^{-1}. The structure of the MEGO–MnO_2 composites was characterized by X-ray diffraction (XRD), using a powder diffractometer (SmartLab, Rigaku, Japan) and Cu K_α radiation. X-ray photoelectron spectroscopy (XPS) was performed on an XP spectrometer (ESCALAB 250, Thermo Scientific, USA) using Al K_α radiation. Raman spectroscopy was performed on a Raman microscope (inVia, Renishaw, UK) using a 532 nm laser. The textural properties of composites were characterized by N_2 adsorption measurement at 77 K (Quantachrome Instruments Autosorb-iQ); the specific surface area and pore size distribution was obtained from absorption/desorption data using a nonlocal density functional theory (NLDFT) method.

2.3 Supercapacitor evaluation

MEGO or MEGO–MnO_2 composite electrodes were fabricated by mixing 87 wt% active material, 10 wt% acetylene black, and 3 wt% polytetrafluoroethylene (PTFE; 5 wt% dispersion in water). The mixture was rolled into a membrane with a thickness of 40–50 μm, then punched into circular electrodes with a diameter of 7 mm, and dried at 80 °C for 12 h in vacuum. The aMEGO electrodes were prepared by a similar procedure using 97 wt% aMEGO and 3 wt% PTFE. Symmetric supercapacitors were assembled with two identical electrodes; asymmetric supercapacitors were assembled using the MEGO–MnO_2 composites as positive electrodes and aMEGO as negative electrodes. A 1 M Na_2SO_4 solution was used as the electrolyte and the supercapacitors were assembled according to the procedures described in previous report.[22] Cyclic voltammetry (CV) and galvanostatic charging–discharging were performed to test the electrochemical performance of the electrodes. Electrochemical impedance spectroscopy (EIS) was conducted in the frequency range of from 100 kHz to 0.01 Hz with an electrochemical station (PARSTAT 4000, Princeton Applied Research, USA). The cycling stability was tested by a battery measurement system (CT2001A, LAND, China). The specific capacitance of an electrode (C), specific capacitance of a SC (C_{cell}), energy density (E), and average power density (P) were calculated from the galvanostatic charge–discharge curves according to the following equations:

$$C = 4It/(mV)$$

$$C_{cell} = C/4$$

$$E = C_{cell}V^2/2$$

$$P = E/t$$

where I is the charge–discharge current, m is the total mass of two electrodes, t is the discharge time, and V is the initial voltage at the beginning of the discharge process.

3.   Results and discussion

As shown in Fig. 1, a self-limited redox reaction between $KMnO_4$ and MEGO was utilized to deposit birnessite-type MnO_2 3D structures on the surface of MEGO. The reaction between carbon and the MnO_4^- ions proceeded according to the following equation:[33]

$$4MnO_4^- + 3C + 2H_2O = 4MnO_2 + 3CO_2 + 4OH^-$$
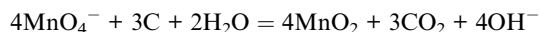
In this reaction, carbon (MEGO) served as a sacrificial reductant and converted $KMnO_4$ to MnO_2, which was deposited on the carbon surface and restricted further reaction between MnO_4^- and carbon, leading to the synthesis of ultrathin MnO_2 sheets.[34–36] The GMn-x ($x = 10, 40, 120$) composite was prepared by immersing MEGO in an aqueous $KMnO_4$ solution to react for 10, 40, or 120 min. The weight percentage of MnO_2 in the MEGO–MnO_2 composites were 17.1, 24.5, and 33.6% for GMn-10, GMn-40, and GMn-120, respectively, as estimated by TGA (Fig. S1†).

Fig. 2 shows SEM images of MEGO and the MEGO–MnO_2 composites. As reported in literature,[31] MEGO powder consisted of reduced graphene oxide platelets with a crumpled but microscopically smooth surface (Fig. 2(a)). After 10 min of reaction, particles were observed on MEGO, forming the rough surface shown in Fig. 2(b). A longer reaction time, *e.g.*, 40 min, resulted in a 3D morphology with sheets lying on the MEGO and
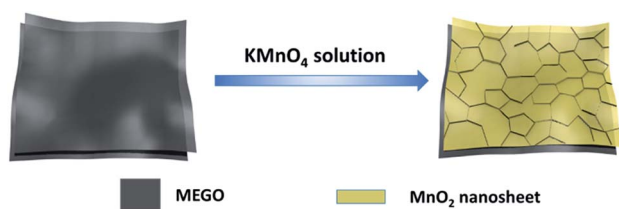

Fig. 1 Schematic illustration of the self-controlled redox reaction used for deposition of 3D MnO_2 structures on MEGO.
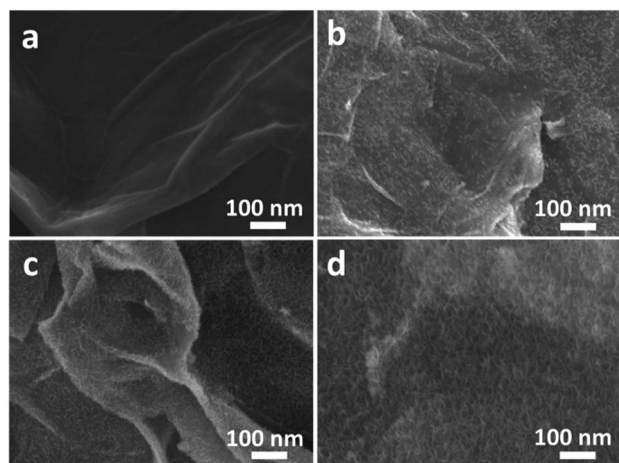
interconnected protruding walls in GMn-40 (Fig. 2(c)). With further increase in the deposition duration, the distribution density and the height of the walls increased dramatically, making the MEGO layers undistinguishable in the SEM image of GMn-120 in Fig. 2(d).

The detailed structure of the MEGO–MnO_2 composites was elucidated by TEM studies. The images in Fig. 3 and S2† show that the MnO_2 nanosheets were strongly anchored on MEGO through the use of ultrasonics during TEM sample preparation without exfoliating. As shown in Fig. S2a and b,† quasi-two-dimensional (quasi-2D) graphene sheets were covered with a thin layer of MnO_2 after 10 min of growth. The slit-like contrast observed in the bright-field TEM images corresponds to the walls protruding from the MEGO planes shown in the SEM images. The TEM image of GMn-40 in Fig. 3(a) shows that the interconnected walls were uniformly distributed on MEGO with clear lattice fringes, which are also shown in the TEM image with higher magnification in Fig. 3(b). The HRTEM image in Fig. 3(c) indicates that the interplanar distance of the walls was 0.7 nm, which is consistent with the interplanar distance of the (001) planes in birnessite-type MnO_2.[37,38] Close inspection of Fig. 3(d) showed that the lattice fringes of the sheets lying on MEGO were distinctly separated by an interplanar distance of 0.24 nm (Fig. 3(d)), corresponding to the (200) planes of MnO_2. Since the (001) plane is perpendicular to the (200) plane in monoclinic birnessite-type MnO_2, it is presumed that the vertical walls were continuously connected to the sheets lying on MEGO in our composites. From the measurements of the wall thickness (Fig. 3(b)), the thickness of MnO_2 sheets was estimated to be in the range of 1–5 nm, which showed little variation even when MnO_2 was deposited over a much longer period. In the case of GMn-120, for example, even though the density and the height of walls were largely increased (Fig. S2c and d†), the thickness of the walls was remained similar. Nitrogen adsorption measurements show that the Brunauer–Emmett–Teller (BET) specific surface area of GMn-40 is ~37 m^2 g^{-1}, slightly larger than ~31 m^2 g^{-1} of MEGO. At the same time the peak of typical pore size distribution in MEGO/MnO_2 composites shifts to a smaller value

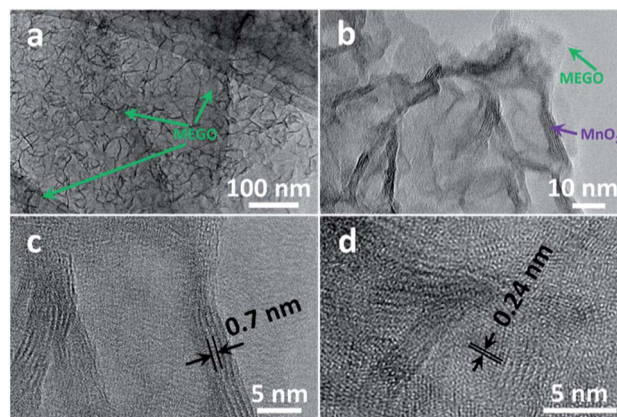Fig. 2 Typical SEM images of (a) MEGO, (b) GMn-10, (c) GMn-40, and (d) GMn-120.

Fig. 3 TEM images of GMn-40 at (a and b) low magnification and (c and d) high magnification.

compared with that of MEGO, which is presumably attributed to the formation of porous MnO_2 3D architectures (Fig. S3†).

XRD, Raman spectroscopy, and XPS were carried out to further verify the phase of MnO_2 in the MEGO–MnO_2 composites, with measurements of bare MEGO used as references. As shown in Fig. 4(a), the MEGO XRD pattern shows two broad peaks at 2θ of around 23° and 43°, which are assigned to the (002) and (100) crystal planes, respectively, of layered carbon. In addition to the strong signals from MEGO in the XRD patterns of the MEGO–MnO_2 composites, three broad diffraction peaks at about 12°, 37°, and 66° can be indexed to birnessite-type MnO_2 (JCPDS card no. 42-1317; space group: $C2/m$ (12)).[28] As the reaction time was increased, the diffraction intensity from MEGO decreased while the intensities of the peaks belonging to MnO_2 became stronger owing to the increasing MnO_2 content in the composites. In the Raman spectra shown in Fig. 4(b), one can clearly identify three bands at 496, 575, and 630 cm^{-1} of the MEGO–MnO_2 composites, in addition to the D band (1350 cm^{-1}) and G band (1590 cm^{-1}) of graphitic carbon. According to previous reports,[39,40] the bands at 496 and 575 cm^{-1} belong to Mn–O stretching vibrations in the basal plane of the MnO_6 sheets, and the band located at 630 cm^{-1} can be assigned to the symmetric stretching vibration of Mn–O in the MnO_6 group in birnessite-type MnO_2.[41] It is worth noting that the intensity ratio of D to G bands (I_D/I_G) of MEGO showed little change after MnO_2 was deposited (Table S1†), indicating that the amount of defects in MEGO was not significantly increased by the reaction with $KMnO_4$. The XPS spectra shown in Fig. 4(c) and (d) further suggest that the predominant oxidation state of Mn was +4 in the composites, as evidenced by Mn $2p_{3/2}$ and Mn $2p_{1/2}$ peaks with a spin-energy separation of 11.8 eV.[42,43]

Fig. 5(a) shows CV curves of symmetric SCs using MEGO or MEGO–MnO_2 composites as active materials in the electrodes. The area under the CV curves obtained at a scan rate of 10 mV s^{-1} increased with reaction time, indicating that the capacitance was enhanced by incorporating pseudocapacitive MnO_2 into MEGO; the increase in MnO_2 loading led to an increase in the area, although GMn-120 showed a very small enhancement
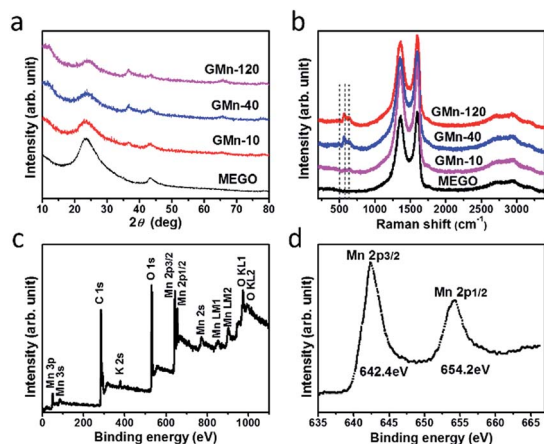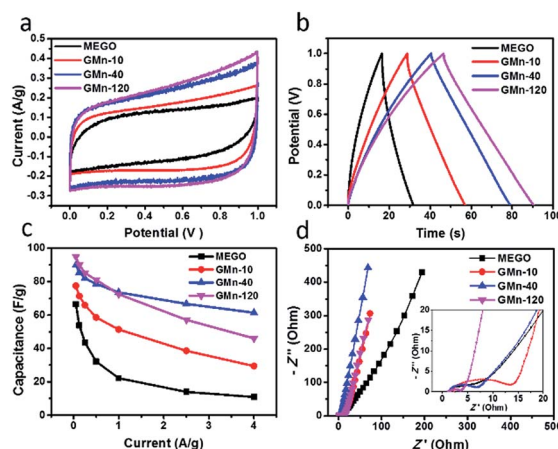

Fig. 5 (a) CV curves obtained at a scan rate of 10 mV s^{-1} and (b) galvanostatic charge–discharge curves obtained at a current density of 0.5 A g^{-1} for MEGO and MEGO–MnO_2 composite electrodes with various MnO_2 loadings. (c) Specific capacitance of MEGO and MEGO–MnO_2 composites versus charge–discharge current density. (d) Nyquist curves of MEGO and MEGO–MnO_2 composites.

compared to GMn-40. The quasi-rectangular shape of the CV curves indicates good capacitive behavior and a fast charging–discharging process in the MEGO–MnO_2 composites. The galvanostatic charging–discharging curves in Fig. 5(b) are all linear and symmetrical, further indicating the reversible feature of the redox reaction and the nearly ideal electrochemical capacitive behavior of samples. Fig. 5(c) shows the specific capacitance of GMn-10, GMn-40, and GMn-120 at various current densities calculated from the discharge curves. While the specific capacitance of the composites increased with the MnO_2 loading in the composite for discharge current densities below 1 A g^{-1}, GMn-40 showed the highest gravimetric capacitance among all composites for discharge current densities above 1 A g^{-1}, suggesting that this was the most optimized performance of GMn-40. Compared to MEGO, the MEGO–MnO_2 composites demonstrated significant improvement in the specific capacitance, which was greatly dependent on the MnO_2 loading and its efficient utilization. We believe the deteriorated rate performance of GMn-120 was caused by the higher MnO_2 vertical walls protruding from the MEGO plane, which may have lengthened the ion-diffusion path in MnO_2 and simultaneously decreased the electrical conductivity between MnO_2 and carbon. The frequency response of the electrodes was further tested by EIS. As shown in the Nyquist plots in Fig. 5(d), GMn-40 showed the most vertical frequency response curves when compared to MEGO or all other MEGO–MnO_2 composites, suggesting highly capacitive behavior.[25,28] The semicircles in the Nyquist plots, as shown in the magnified high-frequency region in the inset of Fig. 5(d), are related to the charge-transfer resistance (R_{ct}) caused by faradaic reactions and the double-layer capacitance.[28,44] R_{ct} was measured to be about 1.5, 6.4, 2.2, and 17 Ω for MEGO, GMn-10, GMn-40, and GMn-120, respectively, further indicating that GMn-40 had the fastest charge-transfer and charge-transport process among the MEGO–MnO_2 composites. The outstanding electrochemical

Fig. 4 (a) XRD patterns and (b) Raman spectra of MEGO and MEGO–MnO_2 composites. (c) XPS survey spectra and (d) XPS Mn 2p spectra of GMn-40.

performance of the GMn-40 electrode was a consequence of the unique 3D MnO_2 architecture on MEGO, with 1–5 nm thin MnO_2 nanosheets on MEGO and balanced density and height of the walls perpendicular to MEGO.

Based on its outstanding performance, GMn-40 was utilized to fabricate symmetric supercapacitors, and their performance in a 1 M Na_2SO_4 electrolyte was investigated in detail. As shown in Fig. S4,† rectangular CV curves were obtained up to a potential of 2.0 V, which is much higher than the working voltage previously reported for MnO_2-based symmetric supercapacitors in aqueous electrolytes.[19,29,30,45] The high working voltage achieved here may be partially explained by the exposed sheet edges of the vertical MnO_2 walls, which provided a large number of active sites for H^+ adsorption and decreased the over potential for gas evolution reactions through the interlayer space.[28] Based on the galvanostatic charge–discharge curves of GMn-40, the working voltage of 2.0 V resulted in an energy density of 14 W h kg^{-1} (13.6 W h L^{-1} based on the electrode density of 0.97 g cm^{-3}) at a power density of 250 W kg^{-1} (243 W L^{-1}) and a maximum power density of 7.67 kW kg^{-1} (7.44 kW L^{-1}) at 5.46 W h kg^{-1} (5.3 W h L^{-1}). The GMn-120 symmetric supercapacitor was also tested at a high working potential of 2 V, but it exhibited low capacitance (Fig. S5†).

GMn-40 was also used for building asymmetric SCs to utilize both faradic reactions and electric-double-layer capacitance in one device.[22,25] In our previous work, a novel carbon material (aMEGO) with high surface area and high capacitance in an organic electrolyte was synthesized using chemical activation of

MEGO.[32] As shown in Fig. S6,† aMEGO also demonstrated good rate performance in a 1 M Na_2SO_4 electrolyte in the current work. With an optimal mass ratio of GMn-40/aMEGO = 1.0 : 1.5 (Fig. S7†), an asymmetric SC using GMn-40 as the positive electrode and aMEGO as the negative electrode (hereafter referred to as GMN-40//aMEGO) was packaged with 1 M Na_2SO_4 as the electrolyte. Fig. 6(a) and (b) show that CV curves of this asymmetric SC maintained rectangular shapes at scan rates from 10 to 200 mV s^{-1} under a voltage of up to 1.8 V. The EIS curve in Fig. 6(d) shows a vertical line in the low-frequency region and a small R_{ct} of about 1.5 Ω. Using the galvanostatic charge–discharge curves shown in Fig. 6(c), the gravimetric capacitance of the asymmetric SC was calculated to be 56 F g^{-1} at a current density of 0.1 A g^{-1} (based on the total mass of active materials in both positive and negative electrodes). Thus, a maximum gravimetric energy density of 25.1 W h kg^{-1} and a power density of 4.9 kW kg^{-1} were obtained from the asymmetric SC (Fig. 6(e)), which are higher than those of symmetric SCs and other MnO_2-based asymmetric SCs (Table S2†). In addition, the asymmetric SCs also exhibited long cycle life, with a capacitance retention of 75% after 5000 charge–discharge cycles at a current density of 1 A g^{-1} (Fig. 6(f)).

4. Conclusions

A MEGO–MnO_2 composite with 3D architecture was synthesized by a self-limited redox reaction between MEGO and $KMnO_4$. The composite consisted of interconnected ultra-thin MnO_2 nanosheets on the surface of MEGO. Owing to the short ion-diffusion paths and reduced electrical conductivity, the utilization efficiency of MnO_2 was improved. It was found that with the optimized MnO_2 loading (24.5 wt%), both symmetric and asymmetric supercapacitors made from the composite exhibited excellent electrochemical performance in 1 M Na_2SO_4. Working under a high voltage of up to 1.8 V, the asymmetric GMn-40//aMEGO supercapacitors delivered a high energy density of 25.1 W h kg^{-1} and exhibited a cycling retention of 75% after 5000 cycles.

Fig. 6 (a) CV curves of GMn-40//aMEGO asymmetric supercapacitor (SC) measured in various potential windows at a scan rate of 20 mV s^{-1} (b) CV curves of the asymmetric SC measured between 0 and 1.8 V at various scan rates. (c) Galvanostatic charge–discharge curves of the asymmetric SC at various current densities. (d) Nyquist plot. (e) Energy density *versus* power density for the asymmetric SC. (f) Cycling stability of the asymmetric SC at a current density of 1 A g^{-1}.

Notes and references

1 J. R. Miller and P. Simon, *Science*, 2008, **321**, 651.
2 P. Simon and Y. Gogotsi, *Nat. Mater.*, 2008, **7**, 845.
3 G. Wang, L. Zhang and J. Zhang, *Chem. Soc. Rev.*, 2012, **41**, 797.
4 L. L. Zhang and X. S. Zhao, *Chem. Soc. Rev.*, 2009, **38**, 2520.
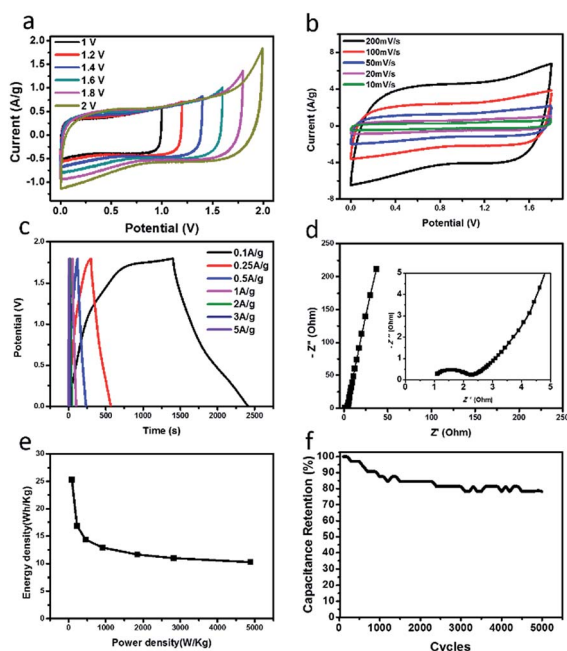5 V. Augustyn, P. Simon and B. Dunn, *Energy Environ. Sci.*, 2014, **7**, 1597.

6 A. Burke, *J. Power Sources*, 2000, **91**, 37.

7 C. C. Hu, K. H. Chang, M. C. Lin and Y. T. Wu, *Nano Lett.*, 2006, **6**, 2690.

8 S. K. Meher, P. Justin and G. R. Rao, *Electrochim. Acta*, 2010, **55**, 8388.

9 P. K. Rajendra and N. Miura, *Electrochem. Commun.*, 2004, **6**, 1004.

10 Z. Yu, B. Duong, D. Abbitt and J. Thomas, *Adv. Mater.*, 2013, **25**, 3302.

11 M. Toupin, T. Brousse and D. Bélanger, *Chem. Mater.*, 2004, **16**, 3184.

12 M. J. Zhi, C. C. Xiang, J. T. Li, M. Li and N. Q. Wu, *Nanoscale*, 2013, **5**, 72.

13 Y. Hou, Y. Cheng, T. Hobson and J. Liu, *Nano Lett.*, 2010, **10**, 2727.

14 M. N. Patel, X. Wang, D. A. Slanac, D. A. Ferrer, S. Dai, K. P. Johnston and K. J. Stevenson, *J. Mater. Chem.*, 2012, **22**, 3160.

15 S. Chen, J. W. Zhu, X. D. Wu, Q. F. Han and X. Wang, *ACS Nano*, 2010, **4**, 2822.

16 K. S. Novoselov, A. K. Geim, S. V. Morozov, D. Jiang, Y. Zhang, S. V. Dubonos, I. V. Grigorieva and A. A. Firsov, *Science*, 2004, **306**, 666.

17 A. K. Geim and K. S. Novoselov, *Nat. Mater.*, 2007, **6**, 183.

18 A. K. Geim, *Science*, 2009, **324**, 1530.

19 L. L. Peng, X. Peng, B. R. Liu, C. Z. Wu, Y. Xie and G. H. Yu, *Nano Lett.*, 2013, **13**, 2151.

20 Q. Cheng, J. Tang, J. Ma, H. Zhang, N. Shinya and L. C. Qin, *Carbon*, 2011, **49**, 2917.

21 W. H. Guo, T. J. Liu, P. Jiang and Z. J. Zhang, *J. Colloid Interface Sci.*, 2015, **437**, 304.

22 X. Zhao, L. L. Zhang, S. Murali, M. D. Stoller, Q. H. Zhang, Y. W. Zhu and R. S. Ruoff, *ACS Nano*, 2012, **6**, 5404.

23 Z. P. Li, J. Q. Wang, S. Liu, X. H. Liu and S. G. Yang, *J. Power Sources*, 2011, **196**, 8160.

24 Z. P. Li, Y. J. Mi, X. H. Liu, S. Liu, S. G. Yang and J. Q. Wang, *J. Mater. Chem.*, 2011, **21**, 14706.

25 Z. J. Fan, J. Yan, T. Wei, L. J. Zhi, G. Q. Ning, T. Y. Li and F. Wei, *Adv. Funct. Mater.*, 2011, **21**, 2366.

26 X. C. Dong, X. W. Wang, J. Wang, H. Song, X. G. Li, L. Y. Wang, M. B. Chan-Park, C. M. Li and P. Chen, *Carbon*, 2012, **50**, 4865.

27 J. G. Wang, Y. Yang, Z. H. Huang and F. Kang, *Carbon*, 2013, **61**, 190.

28 L. Zhao, J. Yu, W. J. Li, S. G. Wang, C. L. Dai, J. W. Wu, X. D. Bai and C. Y. Zhi, *Nano Energy*, 2014, **4**, 39.

29 S. J. He, C. X. Hu, H. Q. Hou and W. Chen, *J. Power Sources*, 2014, **246**, 754.

30 S. J. He and W. Chen, *J. Power Sources*, 2014, **262**, 391.

31 Y. W. Zhu, S. Murali, M. D. Stoller, A. Velamakanni, R. D. Piner and R. S. Ruoff, *Carbon*, 2010, **48**, 2118.

32 Y. W. Zhu, S. Murali, M. D. Stoller, K. J. Ganesh, W. W. Cai, P. J. Ferreira, A. Pirkle, R. M. Wallace, K. A. Cychosz, M. Thommes, D. Su, E. A. Stach and R. S. Ruoff, *Science*, 2011, **332**, 1537.

33 H. Xia, M. Lai and L. Lu, *J. Mater. Chem.*, 2010, **20**, 6896.

34 X. Jin, W. Zhou, S. Zhang and G. Z. Chen, *Small*, 2007, **3**, 1513.

35 X. P. Dong, W. H. Shen, J. L. Gu, L. M. Xiong, Y. F. Zhu, H. Li and J. L. Shi, *J. Phys. Chem. B*, 2006, **110**, 6015.

36 Y. Chen, Y. Zhang, D. S. Geng, R. Y. Li, H. L. Hong, J. Z. Chen and X. L. Sun, *Carbon*, 2011, **49**, 4434.

37 M. N. Patel, X. Wang, B. Wilson, D. A. Ferrer, S. Dai, K. J. Stevenson and K. P. Johnston, *J. Mater. Chem.*, 2010, **20**, 390.

38 M. Huang, Y. X. Zhang, F. Li, L. L. Zhang, R. S. Ruoff, Z. Y. Wen and Q. Liu, *Sci. Rep.*, 2014, **4**, 3878.

39 A. Ogata, S. Komaba, R. Baddour-Hadjean, J. P. Pereira-Ramos and N. K. Doping, *Electrochim. Acta*, 2008, **53**, 3084.

40 J. P. Liu, J. Jiang, C. W. Cheng, H. X. Li, J. X. Zhang, H. Gong and H. J. Fan, *Adv. Mater.*, 2011, **23**, 2076.

41 S. B. Ma, K. Y. Ahn, E. S. Lee, K. H. Oh and K. B. Kim, *Carbon*, 2007, **45**, 375.

42 H. J. Huang and X. Wang, *Nanoscale*, 2011, **3**, 3185.

43 Y. S. Luo, J. Jiang, W. W. Zhou, H. P. Yang, J. S. Luo, X. Y. Qi, H. Zhang, D. Y. W. Yu, C. M. Li and T. Yu, *J. Mater. Chem.*, 2012, **22**, 8634.

44 J. Chang, M. H. Jin, F. Yao, T. H. Kim, V. T. Le, H. Y. Yue, F. Gunes, B. Li, A. Ghosh, S. S. Xie and Y. H. Lee, *Adv. Funct. Mater.*, 2013, **23**, 5074.

45 M. Huang, R. Mi, H. Liu, F. Li, X. L. Zhao, W. Zhang, S. X. He and Y. X. Zhang, *J. Power Sources*, 2014, **269**, 760.